Title

Sodium-glucose transporter 2 is a diagnostic and therapeutic target for early-stage lung adenocarcinoma.

Journal

Science translational medicine, 10(467)

ISSN

1946-6242

Authors

Scafoglio, Claudio R
Villegas, Brendon
Abdelhady, Gihad
et al.

Publication Date

2018-11-14

Data Availability

The data associated with this publication are in the supplemental files.

Peer reviewed

Manuscript Information

Journal name: Science translational medicine
NIHMS ID: NIHMS1011632
Manuscript Title: Sodium-glucose transporter 2 is a diagnostic and therapeutic target for early-stage lung adenocarcinoma
Submitter: Claudio Scafoglio (cscafoglio@mednet.ucla.edu)

Manuscript Files

Type	Fig/Table #	Filename	Size	Uploaded
manuscript		NIHMS1011633-manuscript.docx	189923	2019-02-12 20:12:22
figure	Figure 1	Fig.1_PMC.tif	18165040	2019-02-13 04:51:26
figure	Figure 2	Fig.2_PMC.tif	9014396	2019-02-13 04:24:48
figure	Figure 3	Fig.3_PMC.tif	8110708	2019-02-13 04:51:31
figure	Figure 4	Fig.4_PMC.tif	2984168	2019-02-13 04:51:34
figure	Figure 5	Fig.5_PMC.tif	1506020	2019-02-13 04:51:35
supplement	Supplement	aat5933_Supplement_PMC.docx	2813645	2019-02-13 04:53:58

Sodium-Glucose Transporter 2 is a diagnostic and therapeutic target for early stage lung adenocarcinoma

Authors: Claudio R. Scafoglio[1*], Brendon Villegas[1], Gihad Abdelhady[1], Sean T. Bailey[1,2], Jie Liu[3], Aditya S. Shirali[4], W. Dean Wallace[5], Clara E. Magyar[5], Tristan R. Grogan[6], David Elashoff[6], Tonya Walser[1], Jane Yanagawa[4], Denise R. Aberle[7], Jorge R. Barrio[3], Steven M. Dubinett[1,3,5,8], David B. Shackelford[1*]

Affiliations:
[1]Division of Pulmonary and Critical Care Medicine, David Geffen School of Medicine, University of California Los Angeles, Los Angeles, CA 90095
[2]Lineberger Comprehensive Cancer Center, University of North Carolina at Chapel Hill, Chapel Hill, NC 27514
[3]Department of Molecular and Medical Pharmacology, David Geffen School of Medicine, University of California Los Angeles, Los Angeles, CA 90095
[4]Division of Thoracic Surgery, David Geffen School of Medicine, University of California Los Angeles, Los Angeles, CA 90095

[5]Department of Pathology and Laboratory Medicine, David Geffen School of Medicine, University of California Los Angeles, Los Angeles, CA 90095
[6]Department of Medicine Statistics Core, David Geffen School of Medicine, University of California-Los Angeles, Los Angeles, CA, 90095
[7]Department of Radiological Sciences, David Geffen School of Medicine, University of California Los Angeles, Los Angeles, CA 90095
[8]Department of Medicine, VA Greater Los Angeles Healthcare System, Los Angeles, CA 90073

*To whom correspondence should be addressed:
Claudio R. Scafoglio, MD PhD cscafoglio@mednet.ucla.edu
David B. Shackelford, PhD dshackelford@mednet.ucla.edu

One Sentence Summary: Lung premalignancy and early-stage adenocarcinoma use a mechanism of glucose transport that can be targeted for early diagnosis and treatment.

Abstract: The diagnostic definition of indeterminate lung nodules as malignant or benign poses a major challenge for clinicians. We discovered a potential marker, the sodium glucose transporter 2 (SGLT2), whose activity identified metabolically active lung premalignancy and early-stage lung adenocarcinoma (LADC). We found that SGLT2 is expressed early in lung tumorigenesis and is found specifically in pre-malignant lesions and well-differentiated adenocarcinomas. Of note, SGLT2 activity could be detected in vivo by positron emission tomography (PET) with the tracer methyl-4-[^{18}F] fluorodeoxyglucose (Me4FDG), which specifically detects SGLT activity. Using a combination of immunohistochemistry and Me4FDG PET, we identified high expression and functional activity of SGLT2 in lung premalignancy and early-stage/low-grade LADC. Furthermore, selective targeting of SGLT2 with FDA-approved small molecule inhibitors, the gliflozins, greatly reduced tumor growth and prolonged survival in autochthonous mouse models and patient-derived xenografts of LADC. Targeting SGLT2 in lung tumors may intercept lung cancer progression at early stages of development by pairing Me4FDG PET imaging with therapy using SGLT2 inhibitors.

Introduction

Non-small cell lung cancer (NSCLC) is the leading cause of cancer-related mortality worldwide. Despite the success of targeted and immune-based therapies in NSCLC (*1, 2*), early diagnosis and surgical resection of early-stage disease remain the best opportunity for a cure: the 5-year survival of NSCLC patients is 55.6% for localized disease but only 4.5% for metastatic disease (*3, 4*). However, according to statistics of the NIH Surveillance, Epidemiology, and End Result Program, only 16% of newly diagnosed lung cancers are localized, whereas the majority has already spread to regional lymph nodes or to distant metastatic sites at the time of diagnosis (seer.cancer.gov/statfacts/html/lungb.html). Recently, intensive research efforts have been directed to the elucidation of the molecular mechanisms of pulmonary premalignancy development and progression (*5-7*), to find signatures of premalignancy that can be targeted for early diagnosis and cancer chemoprevention/interception (*8, 9*).

Lung adenocarcinoma (LADC) and squamous cell carcinoma (SqCC) are the most frequent histologic subtypes of NSCLC. The sequence of pre-malignant lesions that leads to the development of SqCC has been extensively described and studied (*10*), because SqCC develops from the respiratory epithelium of large airways that are accessible by bronchoscopy. Conversely, LADC develops mostly within terminal bronchioles and alveoli, which are not readily accessible by bronchoscopy. Therefore, LADC premalignancy has been more elusive; the only pre-malignant lesion known to be a precursor of LADC is atypical adenomatous hyperplasia (AAH), consisting of a localized growth of pre-malignant, cuboidal cells lining the alveolar walls, defined as a lepidic pattern (*3, 11-14*). AAH can progress to adenocarcinoma in situ (AIS) and minimally invasive adenocarcinoma (MIA), both of which are precursors of invasive adenocarcinoma and are also characterized by lepidic growth. AAH, AIS, and MIA can be detected in vivo by high-resolution

computed tomography (CT), typically presenting as pure or predominantly ground-glass nodules (GGNs) (*15-17*). However, CT is not specific, and GGNs can also correspond to benign lesions, such as alveolar inflammation and hemorrhage. Thus, biomarkers to aid the diagnostic definition of GGNs and to identify AAH, AIS, and MIA non-invasively are urgently needed.

An important hallmark of cancer is the increased requirement of glucose (*18, 19*). Glucose is thought to be imported into tumor cells primarily through specific glucose transporters known as GLUTs, which are frequently over-expressed in cancer cells (*20-22*). Glycolytic metabolism is readily imaged in cancer by positron emission tomography (PET) using a glucose analog, 2-[^{18}F] fluorodeoxyglucose (FDG) (*20*). Although FDG PET is a standard tool for staging lung cancer, it has low sensitivity for identifying premalignant GGNs and early invasive disease (*17, 23*). The absence of FDG uptake in AAH and early-stage LADC has been interpreted as a consequence of a slow growth rate and low requirement of glucose (*15, 17, 23, 24*). However, we previously discovered that cancers can take up glucose by using an alternative glucose transport system, the sodium-dependent glucose transporters (SGLTs) (*25, 26*). SGLT-mediated glucose transport is not detected by FDG PET because FDG is not a transport substrate for SGLTs and is selective for only GLUT transporters (*26, 27*).

Here, we present evidence that SGLT2 is a potential marker of pulmonary premalignancy and early LADC. SGLT-dependent glucose uptake can be selectively measured in vivo by PET imaging using the radiotracer methyl-4-[^{18}F] fluorodeoxyglucose (Me4FDG). Me4FDG is a PET tracer transported specifically by SGLTs, and not by GLUTs. This was demonstrated by in vitro studies showing that uptake of FDG can be completely abolished by GLUT inhibitor cytochalasin B and is not sensitive to SGLT inhibitor phlorizin (*26*). Conversely, Me4FDG uptake is completely abolished by phlorizin but is not affected by cytochalasin B, suggesting that Me4FDG cannot be

transported by GLUT (*26*). In vivo, Me4FDG, unlike FDG, cannot cross the blood-brain barrier, because the capillary blood vessels of the blood-brain barrier express GLUTs but not SGLTs (*27*). In human PET scans, we have previously shown that Me4FDG gives no signal in the normal brain, but is readily taken up by glioblastomas, which are typically characterized by microvascular proliferation, disruption of the blood-brain barrier, and SGLT2 expression (*28*). We previously showed SGLT2 expression in human pancreatic and prostate adenocarcinomas (*25*). Here, we demonstrate that LADCs predominantly use SGLT2 to transport glucose in the early stages of carcinogenesis. As tumors progress to advanced, poorly differentiated carcinomas, they up-regulate GLUT-mediated glucose transport, consistent with frequent positivity for FDG uptake. Using Me4FDG PET to image SGLT activity in vivo, we were able to functionally distinguish SGLT2-mediated active transport of glucose from GLUT1-mediated facilitative diffusion of glucose in genetically engineered mouse models (GEMMs) and in patient-derived xenografts (PDXs) of lung cancer. Finally, we showed that SGLT2 may be an effective therapeutic target in early-stage LADC in both GEMM and PDX models. Our results indicate that PET-guided imaging of SGLT2 activity may offer a means to identify metabolically active pulmonary premalignancy and early LADC and thus could guide targeted therapy/cancer interception with SGLT2 inhibitors.

Results

SGLT2 is a glucose transporter specifically expressed in lung premalignancy and well-differentiated cancer

We have previously shown the expression of SGLT2 in human pancreatic and prostate adenocarcinomas (*25*) and in glioblastomas (*28*). Furthermore, SGLT2 expression has been observed in metastatic lung cancers (*29*). To investigate glucose transporter expression in LADC,

we performed IHC staining for SGLT2 and GLUT1 proteins on 58 human LADC samples (stage I-IV) (fig. 1). The specificity of the SGLT2 antibody was confirmed by immunohistochemistry (IHC) in knockout mouse kidneys lacking the SGLT2 protein and by pre-incubation of the antibody with the antigenic peptide (fig. S1A-C). The clinical and pathological features of the patients are presented in table S1, along with the quantification of SGLT2 and GLUT1 staining by IHC. SGLT2 was highly expressed in well-differentiated (lepidic) and moderately differentiated LADC; its expression was reduced in poorly differentiated, solid-growth disease (fig. 1A, upper panels). Conversely, GLUT1 expression was low in well-differentiated LADC and progressively increased in poorly differentiated tumors (fig. 1A, lower panels). Quantification of the IHC signal showed a significant reduction of SGLT2 ($p = 0.001$) and an increase in GLUT1 ($p < 0.001$) staining as the tumor progressed from lepidic (well differentiated) to moderately and poorly differentiated LADC (fig. 1B). We therefore hypothesized that early-stage LADCs rely on SGLT2 for glucose uptake, whereas more advanced tumors rely on GLUT1. We did not observe a significant change in SGLT2 and GLUT1 staining from Stage I to Stage IV cancers (fig. S1D), but samples from stage IA patients had significantly higher expression of SGLT2 ($p = 0.04$) and lower expression of GLUT1 ($p = 0.02$) than samples from all other stages (fig. S1E). This prompted us to hypothesize that SGLT2 expression is an early event in lung cancer development. We investigated SGLT2 and GLUT1 expression in premalignant lung lesions observed in 9 of the 58 patients, whose clinical characteristics are reported in Table 1. In most patients, multiple GGNs were discovered incidentally on CT performed for other reasons, on screening CT, or as synchronous lesions at the time of resection of an invasive LADC (Table 1). We performed IHC on 11 AAH lesions, 3 AIS lesions, and 3 MIA lesions. SGLT2 was not expressed in normal lung alveoli (fig. 1C, upper panel), but was up-regulated in premalignant lesions (fig. 1D, upper panels).

GLUT1 expression was absent in normal alveoli and premalignant lesions (fig. 1C-D, lower panels).

The pattern of IHC staining with SGLT2 in low-grade and GLUT1 in high-grade LADC was confirmed in four patient-derived xenografts (PDXs). PDX #004 was characterized as a predominantly well-differentiated LADC that expressed high SGLT2 and had no GLUT1 expression (fig. 1E, left panels). In PDX #011 and PDX #186, the predominant histology was moderately differentiated LADC that expressed both SGLT2 and GLUT1 (fig. 1E, central panels). Lastly, PDX #013 was characterized as predominantly poorly differentiated LADC that was positive for GLUT1 but negative for SGLT2 (fig. 1E, right panels). Together, these data suggested that SGLT2 is predominantly expressed in human premalignancy and early-stage, well-differentiated LADCs, and as lung tumors progress to advanced and poorly differentiated cancers, they upregulate GLUT1 as the dominant transporter.

PET imaging reveals differential activity of SGLT2 and GLUT1 transporters in LADC

We have previously profiled functional expression of SGLT2 in mouse xenografts of pancreatic, prostate, and brain tumors and have shown that PET imaging with FDG alone fails to comprehensively profile glucose uptake in tumors that express SGLT2 (*25, 28*). To study the functional activity of SGLTs in LADC, we used a conditionally activated *Lox-Stop-Lox Kras*^{G12D}, *p53*$^{lox/lox}$, *Rosa26-Lox-Stop-Lox-Luc* (referred to as KP$_{luc}$) genetically engineered murine model (GEMM), in which tumor induction with adenovirus expressing Cre recombinase simultaneously activates oncogenic Kras^{G12D}, deletes p53, and induces activation of a luciferase reporter enabling bioluminescent imaging of tumors (*30*). In this model, LADCs are induced by inhalation of adenovirus encoding for Cre recombinase. To estimate the activity of GLUTs and SGLTs in

LADC, we performed PET imaging with FDG and Me4FDG in KP_{luc} mice with advanced stage tumors. The same mice were imaged with both tracers on different days. We observed a modest, but significant correlation between FDG and Me4FDG uptake in lung tumors ($r = 0.4966$, $p < 0.0001$), suggesting that advanced carcinomas may use both SGLT2 and GLUT1 for glucose transport (fig. 2A). A closer observation identified a subpopulation of smaller Me4FDG-positive lesions in KP_{luc} mice that were negative for FDG uptake (red box in fig. 2A). Figure 2B shows representative PET/CT scans of a mouse with multiple lung nodules, including a tumor that was dually positive for Me4FDG and FDG (t1) as well as two smaller nodules (t2 and t3). Tumors t2 and t3 were positive for Me4FDG but negative for FDG and were included in the red box in figure 2A. Using 3D rendering of the regions of interest to locate the exact position of the tumor nodules in the lungs (fig. S2A), we correlated the PET signal with tumor histology (fig. S2B) and IHC (fig. S2C). The larger t1 tumor, which was positive for both FDG and Me4FDG uptake, expressed both SGLT2 and GLUT1 (fig. S2C, top panels). Histological analysis shown for the smaller Me4FDG positive tumor t2 confirmed high SGLT2 and low GLUT1 expression (fig. S2C, bottom panels).

We evaluated the minimum detection limit of Me4FDG to detect early-stage lung nodules by calculating the contrast-to-noise ratio (CNR) as described in (*31*). The lung background was evaluated by designing regions of interest corresponding to the normal lungs (fig. S2D). The formulas used for calculating the CNR are described in the Materials and Methods section. We used a stringent cut-off, setting the minimum detection level at lesions with a $CNR \geq 4$. This analysis showed that CNR for Me4FDG is linearly related to lesion size, as expected (fig. S2E). Tumors t2 and t3 in fig. 2B had CNRs of 4.47 and 7.83, respectively. The smallest lesion with a $CNR \geq 4$ for Me4FDG was t2 in fig. 2B, which measured 0.52 mm^3 in volume (1.0 mm diameter). IHC staining of this lesion showed SGLT2 positivity in 71% of the cells. Overall, quantification

of the IHC signal showed that SGLT2 expression correlated with Me4FDG, as expected (fig. 2C). Likewise, GLUT1 expression is correlated with FDG uptake (*22, 32-34*).

The positive correlation between Me4FDG and FDG was not expected, considering the reciprocal pattern of SGLT2 and GLUT1 expression observed in the human specimens (fig. 1). However, upon closer inspection of nodules expressing both SGLT2 and GLUT1, we observed that the majority of advanced carcinomas expressed both transporters, but the two proteins usually did not co-localize in the same cells. Rather, they were observed in different regions of the tumor nodules, highlighting the intra-tumor heterogeneity of glucose uptake (fig. 2D-G). Specifically, we noticed that SGLT2 was expressed in well-differentiated areas of the tumor, whereas GLUT1 was more abundant in poorly differentiated regions, confirming the pattern already observed in human LADC.

We therefore measured the IHC signal in sub-areas of the tumor nodules that could be clearly identified in the H & E staining as purely low-grade or high-grade (fig. S2F). Similarly to human LADC, the lung tumors in KP_{luc} mice show a very heterogeneous morphology, with well- and moderately differentiated areas (fig. S2G) coexisting with poorly differentiated cell clusters (fig. S2H). In many cases, poorly differentiated cells are interspersed within well- and moderately differentiated cells, in a mosaic pattern (fig. S2I). We therefore quantified SGLT2 and GLUT1 expression only in the regions of interest (ROIs) corresponding to clearly discernible areas of the tumors that were purely low-grade (well- or moderately differentiated) or high-grade (poorly differentiated) (fig. S2F). This analysis showed that SGLT2 and GLUT1 expression was negatively correlated. We color-coded the ROIs as red corresponding to high-grade tumor regions and green corresponding to low-grade tumor regions in fig. 2D. Notably, the high-grade ROIs

clustered with a GLUT1 positive signal, whereas low-grade ROIs clustered with a SGLT2 positive signal (fig. 2D).

We next quantified SGLT2 and GLUT1 staining in lung tumors from KP_{luc} mice. IHC staining in Fig. 2E shows adjacent sections of a representative sample stained with antibodies against SGLT2 (upper panel) and GLUT1 (lower panel), and fig. 2F presents the corresponding hematoxylin-eosin (H & E) staining. The area to the left of the blue line is well differentiated and has high SGLT2 and low GLUT1 expression; the region to the right of the blue line is poorly differentiated and shows low SGLT2 and high GLUT1 signal. Quantification of signal intensity in all lung tumors from n = 7 mice showed a significantly higher SGLT2 staining in low-grade areas of the tumors ($p < 0.001$) and higher GLUT1 signal in high-grade areas ($p < 0.001$) (fig. 2G and table S2). This heterogeneity of glucose transport mirrors the heterogeneity observed in human tumors. Human LADCs often present with a mix of well to poorly differentiated tumor cells. We found several instances in which different areas of the same tumor stained with either SGLT2 or GLUT1 in a mutually exclusive pattern (fig. 2H-I). SGLT2 staining was confined to well and moderately differentiated areas, whereas GLUT1 staining was localized in poorly differentiated regions of the same tumor. Taken together, these data show that SGLT2 and GLUT1 represent two independent mechanisms of glucose uptake in cancer cells, with SGLT2 prevalent in low-grade LADC and GLUT1 prevalent in high-grade LADC.

Premalignant and early LADCs predominantly use SGLT2 to transport glucose into tumors

Our data suggested that Me4FDG may detect early LADC lesions that are FDG-negative, yet metabolically active. They also supported the premise that SGLT2 expression is an early event in LADC oncogenic transformation.

In order to identify the stage of lung carcinogenesis in which SGLT2 is first upregulated, we performed serial IHC in KP_{luc} GEMMs 2, 5, and 8 weeks after tumor induction (fig. 3A-D). Premalignant AAH lesions developed in these mice as early as 2 weeks after tumor induction. By week 5, small adenomas were observed, and by week 8 the mice had advanced adenocarcinomas (fig. 3A). Immunohistochemistry showed that SGLT2 expression was highest in premalignant lepidic lesions at week 2 and progressively diminished in early adenomas and in advanced LADC (fig. 3B, upper panels). Conversely, GLUT1 expression was not detectable in early lesions at week 2, but became progressively stronger as the tumors progressed to adenomas and advanced LADC (fig. 3B, lower panels), suggesting an evolution in the pattern of expression of glucose transporters, with SGLT2 exclusively expressed in early stages and both SGLT2 and GLUT1 present in a mosaic pattern in late stages of lung carcinogenesis. Quantification of the signal confirmed a significant decrease in SGLT2 ($p < 0.001$) and increase in GLUT1 ($p = 0.048$) as the tumors became more advanced (fig. 3C-D and table S3).

To better characterize the evolution of SGLT2 and GLUT1 activity during lung tumorigenesis, we performed a time course of repeat Me4FDG and FDG PET imaging on KP_{luc} mice. The first PET scan was performed when lung nodules reached an average size of 7 mm^3, followed by two bi-weekly scans with a total of three time points. Analysis of tracer uptake at different time points showed that Me4FDG was taken up in early lesions, which were mostly negative for FDG (fig. 3E, time point 1). As the tumors progressed and became more advanced, they increased their uptake of FDG, while Me4FDG uptake remained constant, as shown in representative PET/CT imaging (fig. 3E, time points 2 and 3 and fig. S3). Quantification of tracer uptake in all the lung nodules included in the study ($n = 16$ tumors in 7 mice) confirmed that early tumors had high Me4FDG and low FDG uptake, whereas later stage tumors were more

heterogeneous, with a slightly reduced Me4FDG uptake and significant up-regulation of FDG uptake ($p < 0.001$) (fig. 3F-G). These results are consistent with the expression of both transporters in advanced tumors shown in fig. 2E-G and with the positive correlation between Me4FDG and FDG uptake observed in advanced tumors represented in fig. 2A.

Taken together, these data show that early-stage lung adenocarcinomas and pre-malignant lesions express SGLT2 and use only sodium-dependent transport for glucose uptake, whereas more advanced lesions upregulate GLUT1 expression. These results suggest a complex and spatially heterogeneous pattern of glucose uptake that engages both SGLT- and GLUT-dependent glucose transport during LADC progression (fig. 3H-I).

Gliflozins suppress growth of early stage LADC and extend survival in KP_{luc} GEMMs

Because we observed only SGLT-dependent glucose uptake in early-stage lung nodules, we hypothesized that SGLT2 is required for tumor growth in the early stages of lung carcinogenesis. Therefore, we reasoned that pharmacological inhibition of SGLT2 would slow tumor development in KP_{luc} GEMMs and extend overall survival. Gliflozins are FDA-approved drugs for the treatment of diabetes (*35, 36*) and have been tested against pancreatic cancer in xenografts (*25*). Gliflozins function by inhibiting glucose reabsorption in the kidneys, resulting in significant ($p < 0.01$) excretion of Me4FDG in the urine (fig. 4A-B). We first confirmed that gliflozins were selective inhibitors of SGLT2 activity by performing Me4FDG PET imaging on KP_{luc} mice, with or without co-administration of a single intravenous dose of the SGLT2 inhibitor dapagliflozin (*25, 37*). As anticipated (*25, 38*), dapagliflozin reduced Me4FDG uptake in the tumors, as well as in the heart, liver, and skeletal muscle (fig. 4A-B).

We then performed preclinical studies on KP_{luc} mice to test the SGLT2 inhibitor canagliflozin, which was recently approved by the FDA for diabetes and reported to be a more effective SGLT2 inhibitor than dapagliflozin (*39*). We started treatment with canagliflozin (30 mg/kg/d by oral gavage) (*25*) two weeks after tumor induction, when only premalignant lesions were present (fig. 3A-B). We performed two experiments: in the first trial we treated mice for 6 weeks, followed by sacrifice and histological analysis of lungs and tumors (n = 12 mice per group); in the second trial we treated mice for up to three months for survival analysis (n = 15 mice per group) (fig. 4C). Tumor burden, estimated by bioluminescence imaging (BLI), was significantly lower ($p < 0.001$) in the treatment than the placebo group (fig. 4D-E). Quantification of the BLI signal for both treatment groups up to week 8 showed that canagliflozin significantly delayed the onset of tumors compared to the placebo group ($p < 0.001$). Additionally, plotting the BLI for individual animals up to the end of the trial at week 14 showed that the BLI signal remained lower in the treatment group as compared to the placebo group (fig. S4A). The BLI values of individual mice in the survival and the week 8 cohort are presented in table S4 and S5, respectively. Histological analysis of the lungs and measurement of tumor area confirmed that canagliflozin treated mice had a significantly lower tumor burden than in the placebo group ($p < 0.05$), both at 8 weeks and in the survival cohort (fig. 4F-G). A Ki67 stain of the mouse tumors showed a significantly lower ($p = 0.001$) proliferation rate in the canagliflozin treatment group compared with that in the placebo group, but only in premalignant lesions (fig. 4H-I) and not in solid LADC (fig. S4B-C), suggesting that SGLT2 inhibition may target premalignant lesions with higher efficacy than advanced carcinomas. This is consistent with the observation that SGLT2 is expressed predominantly in early lesions.

Overall, canagliflozin treatment significantly prolonged mouse survival ($p = 0.0003$) compared with the placebo group (fig. 4J). However, tumors eventually escaped SGLT2 inhibition and formed large tumor masses even within the canagliflozin group (fig. 4F). We analyzed SGLT2 expression in the lungs of mice from both treatment groups and showed that SGLT2 expression was low in the placebo group, with only 17% of tumor cells staining positive for SGLT2, consistently with the advanced nature of these tumors. Tumors in the canagliflozin group had significantly higher SGLT2 expression ($p < 0.0001$): 30% of the tumor cells had positive SGLT2 staining (fig. S4D-E). This suggests that over-expression of the transporter may be a compensatory mechanism induced by SGLT2 inhibition. Taken together, these data suggest that SGLT2-mediated glucose transport is an early requirement for lung carcinogenesis and may sustain the increased proliferation rate associated with progression from premalignancy to invasive cancer and tumor growth.

Me4FDG PET-guided inhibition of SGLT2 activity in LADC reduced tumor growth in patient-derived xenografts

We next performed a therapeutic trial with canagliflozin (30 mg/kg/d by oral gavage for one month) (*25*) in the same four PDXs presented in fig. 1E to test the relevance of targeted SGLT2 inhibition in human cancers (fig. 5). Mice were imaged by Me4FDG and FDG PET/CT before treatment and 2 weeks after starting treatment. Weekly CT scans were acquired to monitor tumor burden. The mice were sacrificed and the tumors analyzed after 1 month of treatment (fig. 5A). Overall, we observed a significant ($p = 0.003$) reduction in tumor volumes in the treatment group compared with the placebo group. Treated mice had final tumor volumes approximately 47% lower

than the control mice (geometric mean ratio 0.53, 95% CI: 0.36-0.80, p = 0.003), after adjusting for trial and mouse random effects (fig. 5B).

Despite the variability in SGLT2 staining between moderately and poorly differentiated PDXs shown in fig. 3E, all four PDXs displayed a detectable uptake of Me4FDG and a similar response to SGLT2 inhibition (fig. 5C-D). This was expected, considering that these PDXs were not purely SGLT2-positive or SGLT2-negative, but in each PDX well and moderately differentiated, SGLT2-positive areas coexisted with poorly differentiated, SGLT2-negative areas of the same tumor (fig. S5).

Overall, Me4FDG uptake increased from day 0 to day 14 in the placebo group, whereas canagliflozin significantly reduced Me4FDG uptake ($p < 0.001$), as expected (fig. 5C-D). Notably, Me4FDG uptake before treatment in the placebo group significantly correlated with tumor volume fold change from the beginning to the end of the trial ($p < 0.001$), confirming an important role of SGLT2-dependent glucose uptake in the regulation of tumor growth (fig. 5E). In the canagliflozin group, Me4FDG scans before treatment showed no significant correlation with tumor volume fold change (fig. 5F). Moreover, the percent reduction of Me4FDG uptake observed after canagliflozin treatment negatively correlated with the fold increase in tumor volume ($p = 0.027$), confirming that a reduction in Me4FDG uptake after treatment can be used as a marker of response to SGLT2 inhibition (fig. 5G). In contrast, FDG signal did not significantly change from day 0 to day 14 in either the placebo or the canagliflozin group (fig. 5H-I). In addition, pre-treatment uptake or changes in FDG uptake between pre- and post-treatment did not correlate with the fold change in tumor volume (fig. 5J-L). These data support the premise that SGLT2 inhibition may be effective in retarding the growth of early lesions that rely on SGLT2 for glucose uptake and that Me4FDG may be used to evaluate the response to therapeutic inhibition of SGLT2.

Discussion

In this study we present evidence that sodium-dependent glucose transporter 2 (SGLT2) is a glucose transport mechanism specifically active in pulmonary pre-malignant lesions and in early LADC. We show expression of SGLT2 protein by IHC with specific antibodies in human LADC specimens, in genetically engineered murine models, and in patient-derived xenografts of LADC. We also report SGLT2-dependent uptake of the PET tracer Me4FDG in vivo both in genetically engineered and in patient-derived murine models. Finally, we confirm that SGLT2 inhibitors delay LADC development and growth in murine models, suggesting SGLT2 inhibition as a potential therapeutic strategy for pre-malignant and early stage LADC. Our data highlight the importance of sodium-dependent glucose transport in early stages of LADC development, both in human tumors and in murine models.

Our data suggest that there is a progression of glucose transporter expression during LADC carcinogenesis: early-stage lesions express only SGLT2, whereas more advanced lesions display a spatially complex and heterogeneous pattern of SGLT2 and GLUT1 expression. Consistently, early-stage tumors accumulate only Me4FG and not FDG, whereas advanced tumors take up both tracers. SGLT2 is most prominent in well-differentiated tumor cells, whereas GLUT1 becomes prevalent in poorly differentiated tumor cells. The mechanisms that drive this evolution in glucose transport in cancer are unknown and will need to be the subject of future investigations. However, we hypothesize that hypoxia is a major driver of the transition from SGLT2- to GLUT1-dependent glucose uptake in LADC. Hypoxia inducible factor 1α (HIF1α) up-regulates GLUT1 expression (*40-42*). We therefore speculate that pre-malignant and early-stage lesions, which are well oxygenated and perfused, preferentially express SGLT2. In contrast, it may be that in advanced hypoxic lesions, GLUT1-mediated glucose transport dominates the tumor landscape.

The discovery of SGLT2 expression in pulmonary premalignancy and early LADC has important diagnostic and therapeutic applications. The National Lung Screening Trial (NLST) has shown that low-dose helical computed tomography (CT) in older, high-risk smokers can reduce lung cancer-related mortality by 20% compared with chest X-ray (*43*). However, CT imaging lacks specificity in distinguishing benign from malignant solitary pulmonary nodules (*44*). Moreover, high-resolution CT has increased the detection rates of indeterminate lung lesions (*45*), including both benign lesions and premalignant or early adenocarcinomas (*46-48*), which require additional imaging or invasive procedures for diagnosis. FDG PET has proven to be ineffective in identifying premalignancy or early LADC (*17, 23*), particularly in the setting of subsolid nodules (*15-17*) such as AAH, AIS, or MIA lesions (*3, 14*). Notably, 73% of patients in the NLST with benign lesions required invasive diagnostic procedures (*49*). In addition to the costs and potential complications associated with these procedures, a quality of life (QOL) study on the impact of low-dose CT (LDCT) screening found that 46% of patients reported psychological distress while awaiting imaging results (*50*). This is particularly notable when considering that 16% of lesions identified on baseline screening LDCT in the NLST were ground-glass opacities that demonstrated relatively constant annual rates of lung cancer diagnosis over the course of six years of follow-up. Subsolid lung nodules commonly represent the early spectrum of LADC and may persist for years before malignant progression. Improved diagnostic tools could potentially reduce cost, invasive procedures, and radiation exposure, as well as improve QOL for patients with indeterminate lung nodules requiring surveillance. In addition to GGNs identified incidentally or by screening, it is common to detect multiple GGNs in patients who undergo surgery for an invasive LADC; Me4FDG PET could aid the follow-up of these lesions and help predict the risk of progression to invasive cancer.

We present evidence that in premalignant and early lepidic lesions, cellular glucose uptake occurs via SGLT2 rather than GLUT1 to satisfy metabolic demands. Therefore, it is anticipated that measurement of SGLT-mediated glucose utilization with the tracer Me4FDG will be valuable in classifying subsolid nodules as benign disease or early lesions within the spectrum of adenocarcinoma. This has the potential to answer an unmet need in the field of lung cancer that CT and FDG PET alone cannot address. Our next goal is to extend this work to clinical trials to evaluate Me4FDG for the diagnostic characterization of indeterminate lung nodules and GGNs and for predicting the clinical behavior of these lesions.

We have also shown that SGLT2 inhibitors hinder tumor progression by limiting glucose supply in cancer cells and that Me4FDG can be used to evaluate the response of LADCs to SGLT2 inhibition by PET imaging before and after receiving treatment. Specific SGLT2 inhibitors (gliflozins), which are FDA-approved for the treatment of diabetes, function by lowering the renal threshold for glucose reabsorption and therefore induce glycosuria and reduce blood glucose in diabetic patients (*35, 36*). We have previously shown that gliflozins have antitumor activity against pancreatic tumors in a xenograft model (*25*). Here, we found that gliflozins specifically target lung premalignancy, effectively reduce tumor burden, and prolong survival if administered at an early stage. Of note, our studies in PDX models treated with canagliflozin showed that Me4FDG uptake before treatment correlated with tumor volume fold decrease after treatment. This suggests that Me4FDG PET imaging could help identify individuals with premalignancy or early LADC with active SGLT2 transporters. In this context, gliflozin therapy could be applied as a cancer interception strategy to prevent or delay malignant progression of subsolid lesions detected by Me4FDG PET and CT (*8, 9*). This strategy would serve patients with other tobacco-associated cardiopulmonary diseases who are poor candidates for surgical resection. The ability to reliably

detect premalignant and early stage lung adenocarcinomas with the use of Me4FDG PET could enable more timely interventions, interrupting the progression to invasive, more advanced disease and thus improving long-term outcomes.

Finally, we observed that Me4FDG PET, by detecting SGLT-dependent glucose transport in vivo, can be used to assess response to treatment with SGLT2 inhibitors. In particular, measurement of Me4FDG uptake in PDXs before and after beginning gliflozin treatment allowed us to establish an inverse correlation between the reduction in Me4FDG uptake as a consequence of the treatment and the rate of tumor volume increase. In patients with FDG-avid tumors, monitoring metabolic responses to drug therapy can be relevant for prognostic assessment and clinical decision-making regarding treatment (*51-53*). Me4FDG PET in mice showed similar if not better minimal detection limits in early stage lesions compared to FDG PET and would be expected to perform in an equivalent manner in humans (*54*). Therefore, we anticipate that PET measurement of SGLT activity in lung premalignancy and adenocarcinomas before and after the beginning of treatment will provide an invaluable precision medicine tool to evaluate the response of pre-malignant lesions to SGLT2 inhibitors.

This study has some limitations. First, we were not able to demonstrate a significant correlation between SGLT2 expression and tumor stage. This is probably due to the low number of samples, especially considering that most surgical samples in the UCLA tumor bank were from early-stage tumors, with relatively low number of advanced LADCs. However, we were able to find a specific profile of SGLT2 expression in lepidic and well-differentiated lesions. Second, we demonstrated Me4FDG uptake in GEMMs and in PDXs but not in LADC patients; this will be the focus of our next studies. Third, we cannot exclude that the effect of SGLT2 inhibitors on tumor volume and mouse survival is due to a systemic effect of lowering blood glucose rather than to the

inhibition of glucose uptake in the tumor. The conditional knockout of SGLT2 in the KP model will discriminate between these two possibilities, and is the focus of our future investigations.

Materials and Methods

Study Design

Purpose of this study was to evaluate SGLT2 as a diagnostic and therapeutic target for early-stage lung cancer. We validated this by immunohistochemistry in human LADC specimens and by PET imaging and therapeutic trials in mouse models. For the immunohistochemistry in human specimens, purpose of the analysis was to assess the correlation between SGLT2 expression and tumor grade and stage. Samples of lung adenocarcinoma were retrospectively selected from the UCLA lung tumor bank according to the pathologic grade and stage. The quantification of the signal was performed blindly by a board-certified pathologist (W. D. W.) using the Aperio ImageScope software. For the imaging and therapeutic trials in mouse models, we used a $Kras^{G12D}$-driven, p53-null GEMM and patient-derived xenografts of human LADC in Non-obese diabetic (NOD), Severe combined immunodeficiency (SCID), interleukin 2 receptor Gamma knockout (NSG) mice. Mice were stratified to make the treatment groups comparable for mouse age (22.3 ± 0.54 weeks), sex (63% female, 47% male), body weight (33.5 ± 0.66 grams), and tumor burden (estimated by bioluminescence signal in the GEMMs and by volumetric determinations from CT scans in PDXs). To determine the group size, we used a generalized estimating equation (GEE) model (*56*) to compare tumor size curves over time and assuming a two-sided 0.05 level of significance. With 12 mice per group we calculated 86% power; therefore, for our therapeutic trials we used groups of at least 12 mice. The tumor burden in the experimental groups was evaluated

by objective measurements: 1) for the GEMMs, weekly bioluminescence measurements throughout the study; 2) for the PDXs, measurement of tumor volumes from CT scans, performed by designing blindly regions of interest encompassing the whole tumor volume; 3) measurement of tumor area by Definiens software in histologic lung sections stained with hematoxylin and eosin.

Mouse models

All experiments performed in mice were approved by the University of California Los Angeles Institutional Animal Care and Use Committee and were carried out according to the guidelines of the Department of Laboratory Animal Medicine at UCLA. All mice were housed in pathogen-free facilities at UCLA.

Genetically engineered mouse model. For our imaging and therapeutic trials in genetically engineered mouse models, we used *Lox-Stop-Lox* $Kras^{G12D}$, $p53^{lox/lox}$, *Rosa26-Lox-Stop-Lox-Luc* mice previously established in our lab, inbred on an FVB background. The mice were bred in our colony at UCLA. Lung tumors were induced by intranasal administration of Adeno-Cre (purchased from University of Iowa adenoviral core) as previously described (*30*). After tumor induction, the tumor burden was estimated by weekly bioluminescence performed on an IVIS Spectrum in vivo imaging system (Perkin Elmer) 10 minutes after intraperitoneal injection of luciferin (150 mg/kg).

Patient-derived xenografts (PDXs). The tumor samples were obtained from surgically resected specimens after informed consent under the UCLA Lung SPORE (PDX #004 and #011) or the Long Beach Memorial Hospital IRB protocol (PDX #013). One of the PDXs (#186) was purchased from Jackson Laboratories. PDXs were established and passaged in NSG mice. NSG mice were procured from the UCLA Radiation Oncology breeding colony. For each mouse, two small pieces of tumor tissue (~2 mm^3) were implanted subcutaneously in the flank regions.

MicroPET imaging

For the PET imaging experiment in the genetically engineered mouse model presented in fig. 2, the mice were scanned 12 weeks after the Adeno-Cre inhalation (1/200 dilution). For the time-course imaging in fig. 3E-G, the mice received a much lower dilution of AdenoCre (1/10,000), and the mice were imaged when the average lung nodule maximum diameters were around 7 mm. For the microPET in patient-derived xenografts, a subset of the mice (PDXs #004, #013, and #186) received both Me4FDG and FDG PET scans the day before and 2 weeks after the beginning of treatment, to evaluate the response of glucose transporter activity to the treatment.

The animals were anesthetized with 1.5% (vol/vol) isoflurane in oxygen, were given a dose of 100 μCi Me4FDG or FDG via tail vein injection, and were maintained under anesthesia for 1 hour of unconscious uptake. The mice were then immobilized on the imaging bed and received a 10 min static PET scan followed by CT scan. Each mouse received two different PET scans with the two tracers (Me4FDG and FDG), on consecutive days to allow for tracer decay. The equipment used was Focus 220 microPET scanner (Concorde Microsystems) and Inveon microPET scanner (Siemens) for the microPET scans, and CrumpCAT (UCLA Crump Institute) for the microCT.

The PET data were analyzed with Amide software version 1.0.4 (amide.sourceforge.net/) (*55*). Regions of interest for the measurement of tumor uptake were drawn corresponding with single lung nodules as identified by CT images. For the GEMMs, which typically present with small intrathoracic nodules with regular shape, ellipsoid ROIs were considered to be an acceptable approximation of tumor volume. For advanced lung nodules which did not have perfectly ellipsoid shape and smooth borders, the ROIs were placed in the center of the tumor nodule, to include as much tumor volume as possible inside the ROI. To compare FDG and Me4FDG uptake, the same ROIs were used in the same mice scanned with the two different tracers, such that comparable tumor volumes were measured with the two tracers. For the PDXs, which typically show larger

and irregularly shaped tumors, isocontour regions of interest were designed based on the CT scans to encompass the whole tumor volumes. The percentage of injected dose for each ROI was calculated by dividing the measured activity in the ROI by the total injected dose, as measured from the PET image by designing an ROI encompassing the whole mouse. The analysis of signal to noise ratio in the mouse nodules was performed as described in (*31*). Briefly, we evaluated the background signal for each mouse by designing a region of interest corresponding to the normal lung (fig. S2D). We then calculated the contrast to noise ratio (CNR) for each nodule by using the following formula (*31*):

$$CNR \approx C_l \times \sqrt{n_l} \times SNR_{pixel} \quad (1)$$

where C_l is the lesion to background contrast, n_l is the number of pixels in the region of interest, and SNR_{pixel} is the signal to noise ratio for a single pixel in the background:

$$C_l = \frac{S_l - S_b}{S_b} \quad \text{and} \quad SNR_{pixel} = \frac{S_b}{\sigma_b} \quad (2)$$

The smallest lesion activity that can generate a CNR greater than 3–5 is called the minimum detectable activity. For the purpose of this analysis, we considered a CNR ≥ 4 as specific signal.

Therapeutic studies in mice

Genetically engineered mouse model. Tumors were induced in KP_{luc} mice by inhalation of Adeno-Cre (1/10 dilution). Two independent trials were performed, starting two weeks after tumor induction. In the first trial (n = 12 mice per group), mice were treated for 6 weeks and then sacrificed for lung collection and fixation in formalin. In the second trial (n = 15 per group), mice were treated until death for survival analysis. The two therapeutic groups were: 1) placebo, receiving daily oral gavage with vehicle: 0.5% hydroxypropyl-methyl cellulose; 2) canagliflozin, receiving a daily dose of canagliflozin (30 mg/kg via oral gavage), as previously described (*25*).

In the survival cohort, two mice (#3416 and #3418) were censored on day 45 and 57, respectively, for esophageal rupture due to complication of the oral gavage.

Patient-derived xenografts. The mice were randomized in two therapeutic groups (same as for the trials in GEMMs): placebo and canagliflozin (30 mg/kg/d). The number of mice per group was 4 for PDX #011, 8 for PDX #013, 3 for PDX #004, and 5 for PDX #186; each mouse was inoculated with two tumors (one tumor on each flank); some of the tumors of PDX #011 developed soft tissue metastases in the axillary regions, and these were counted as separate tumors. Overall, 38 tumors were included in the placebo and 39 tumors in the canagliflozin group. The mice were treated for one month, then sacrificed, and the tumors collected for histology and IHC. The mice of PDX #011 were treated only for 2 weeks, because extremely rapid tumor growth in the placebo group required premature sacrifice of the animals. The tumor volumes at 2 weeks were counted as final tumor volumes.

Immunohistochemistry

For the GEMMs, the mouse lungs were collected and inflated with 10% formalin in phosphate-buffered saline, then incubated in formalin for 24 hours. For the PDXs, subcutaneous tumors were collected and incubated in formalin for 24 hours. All tissues were paraffin-embedded and sliced into 4-µm sections in the Translational Pathology Core Laboratory (TPCL) at UCLA. For human lung cancer samples, tissue blocks were obtained anonymously from the UCLA Lung SPORE tissue bank and from Long Beach Memorial Hospital.

For IHC staining, the slides were de-paraffinized by overnight incubation at 65ºC followed by rehydration by serial passages in xylenes (3 washes of 5 minutes in 100% xylenes) and decreasing concentrations of ethanol (2 washes in 100% ethanol, 2 in 95%, 1 in 80%, 1 in 70%, 1 wash in water). Antigen retrieval was performed for 20 min in 10 mM Tris-HCl, 1 mM EDTA (pH

8.0) for SGLT2 and GLUT1 antibodies, and in 10 mM citrate (pH 6.0) for Ki67. Blocking was performed with 5% goat serum for 1 hour at room temperature, followed by incubation with primary antibodies overnight at 4ºC. Incubation with biotin-labeled secondary antibody was performed at room temperature for 1 hour, followed by incubation with avidin-biotin peroxidase complex (ABC, Vector Labs) and ImmPACT DAB (Vector Labs) for 1 minute. Counterstain was performed with Harris' hematoxylin diluted 1:5 in water. For SGLT2, two different antibodies were used: Abcam ab85626 (1:1000) for mouse tissues, and Novus Biologicals NBP1-92384 (1:250) for human and mouse tissues. The antigenic peptide for the Novus antibody is FHEVGGYSGLFDKYLGAATSLTVSEDPAVGNISSFCYRPRPDSYHLL; for the Abcam antibody the sequence is proprietary, but included in residues 250-350 of human SGLT2. For GLUT1, the Alpha Diagnostics GT11A antibody (1:200) was used. For Ki67, the Thermo Scientific SP6 antibody (1:200) was used.

After the staining, digital images of the slides were obtained with the Aperio ScanScope slide scanner (Leica Biosystems). For the mouse tissues, the IHC signal was quantified with the Definiens Tissue Studio software. For the human tissues, the quantification was performed blindly by a board-certified pathologist (W. D. W.) using the Aperio ImageScope software.

Statistical analyses

The association between SGLT2 expression and Me4FDG uptake in mouse tissue was assessed using a generalized estimating equation (GEE) model (*56*) to accurately account for the same mouse being measured multiple times (multiple tumors per mouse or same mouse over time). We ran a similar model for testing the association between SGLT2 and GLUT1 expression. The associations were also quantified using Pearson's correlation coefficient. The association between

time (weeks 2, 5, 8) and SGLT2 (or GLUT1) was formally assessed using the Jonchkeere-Terpstra test for ordered alternatives.

For the human samples, SGLT2 expression was computed using a weighted average, where each staining score assigned by the Aperio software (3+: very strong; 2+: strong; 2+: light; 1+: very light; 0: no signal) was multiplied by the corresponding percentage of cells in each sample. We then assessed the directional association between morphology categories (lepidic – moderately differentiated – poorly differentiated) and SGLT2 or GLUT1 score using the Jonchkeere-Terpstra test. Statistical analyses were performed using SPSS V24.

For the therapeutic trials in the GEMMs, tumor growth curves (slopes) were compared between canagliflozin and control groups using GEE models (*56*) with terms for time, group, and the time by group interaction. These models also included a random effect for mouse to account for the repeated observations of tumor size over time. We used log transformations to normalize the tumor size outcomes. For the therapeutic trials in PDXs, a linear mixed effects model for log tumor volume was used, with terms for fixed effects (treatment group) and random effects (PDX trial; mice within trial clustered random effect: 38-39 distinct tumors in 20 distinct mice). The data analysis was performed using *proc mixed* from the software SAS V9.4. All other group comparisons were performed using the two-sample t-test unless otherwise noted. P-values < 0.05 were considered statistically significant throughout the manuscript.

Supplementary Materials

Fig. S1. Immunohistochemistry with SGLT2 antibody

Fig. S2. Quantification of tracer uptake and protein expression in lung tumors of KP_{luc} mice

Fig. S3. Time course of PET/CT imaging with Me4FDG and FDG in KP_{luc} mice

Fig. S4. Therapeutic trial with canagliflozin in KP_{luc} mice

Fig. S5. Heterogeneity of morphology and glucose transporter expression in patient-derived xenografts

Table S1. Clinical and pathological features of the 58 lung adenocarcinoma samples included in the study

Table S2. Quantification of SGLT2 and GLUT1 expression in low- and high-grade LADC in GEMMs

Table S3. Time course analysis of SGLT2 and GLUT1 expression in LADC in GEMMs

Table S4. Bioluminescence imaging of the mice included in the SGLT2 inhibition trial (survival cohort)

Table S5. Bioluminescence imaging of the mice included in the SGLT2 inhibition trial (week 8 cohort)

References and notes

1. J. Remon, B. Besse, Immune checkpoint inhibitors in first-line therapy of advanced non-small cell lung cancer. *Curr Opin Oncol* **29**, 97-104 (2017).
2. H. I. Assi, A. O. Kamphorst, N. M. Moukalled, S. S. Ramalingam, Immune checkpoint inhibitors in advanced non-small cell lung cancer. *Cancer* **124**, 248-261 (2018).
3. W. Weichert, A. Warth, Early lung cancer with lepidic pattern: adenocarcinoma in situ, minimally invasive adenocarcinoma, and lepidic predominant adenocarcinoma. *Curr Opin Pulm Med* **20**, 309-316 (2014).
4. H. Kadara, M. Kabbout, Wistuba, II, Pulmonary adenocarcinoma: a renewed entity in 2011. *Respirology* **17**, 50-65 (2012).
5. S. Sivakumar *et al.*, Genomic Landscape of Atypical Adenomatous Hyperplasia Reveals Divergent Modes to Lung Adenocarcinoma. *Cancer Res* **77**, 6119-6130 (2017).
6. J. C. Tsay *et al.*, Molecular characterization of the peripheral airway field of cancerization in lung adenocarcinoma. *PLoS One* **10**, e0118132 (2015).
7. A. Spira *et al.*, Precancer Atlas to Drive Precision Prevention Trials. *Cancer Res* **77**, 1510-1541 (2017).
8. A. Albini, A. DeCensi, F. Cavalli, A. Costa, Cancer Prevention and Interception: A New Era for Chemopreventive Approaches. *Clin Cancer Res* **22**, 4322-4327 (2016).
9. E. H. Blackburn, Cancer interception. *Cancer Prev Res (Phila)* **4**, 787-792 (2011).
10. A. T. Ooi *et al.*, Molecular profiling of premalignant lesions in lung squamous cell carcinomas identifies mechanisms involved in stepwise carcinogenesis. *Cancer Prev Res (Phila)* **7**, 487-495 (2014).
11. Y. Yatabe, A. C. Borczuk, C. A. Powell, Do all lung adenocarcinomas follow a stepwise progression? *Lung Cancer* **74**, 7-11 (2011).

12. W. D. Travis *et al.*, The 2015 World Health Organization Classification of Lung Tumors: Impact of Genetic, Clinical and Radiologic Advances Since the 2004 Classification. *J Thorac Oncol* **10**, 1243-1260 (2015).
13. W. D. Travis *et al.*, International Association for the Study of Lung Cancer/American Thoracic Society/European Respiratory Society: international multidisciplinary classification of lung adenocarcinoma: executive summary. *Proc Am Thorac Soc* **8**, 381-385 (2011).
14. H. Y. Lee *et al.*, Pure ground-glass opacity neoplastic lung nodules: histopathology, imaging, and management. *AJR Am J Roentgenol* **202**, W224-233 (2014).
15. K. Higashi *et al.*, Fluorine-18-FDG PET imaging is negative in bronchioloalveolar lung carcinoma. *J Nucl Med* **39**, 1016-1020 (1998).
16. T. W. Huang *et al.*, Positron emission tomography in bronchioloalveolar carcinoma of the lung. *Eur J Surg Oncol* **38**, 1156-1160 (2012).
17. H. B. Wu *et al.*, Adenocarcinoma with BAC features presented as the nonsolid nodule is prone to be false-negative on 18F-FDG PET/CT. *Biomed Res Int* **2015**, 243681 (2015).
18. O. Warburg, On the origin of cancer cells. *Science* **123**, 309-314 (1956).
19. M. G. Vander Heiden, L. C. Cantley, C. B. Thompson, Understanding the Warburg effect: the metabolic requirements of cell proliferation. *Science* **324**, 1029-1033 (2009).
20. V. Ganapathy, M. Thangaraju, P. D. Prasad, Nutrient transporters in cancer: relevance to Warburg hypothesis and beyond. *Pharmacology & therapeutics* **121**, 29-40 (2009).
21. K. Adekola, S. T. Rosen, M. Shanmugam, Glucose transporters in cancer metabolism. *Curr Opin Oncol* **24**, 650-654 (2012).
22. J. Goodwin *et al.*, The distinct metabolic phenotype of lung squamous cell carcinoma defines selective vulnerability to glycolytic inhibition. *Nat Commun* **8**, 15503 (2017).
23. V. Ambrosini *et al.*, PET/CT imaging in different types of lung cancer: an overview. *Eur J Radiol* **81**, 988-1001 (2012).
24. C. S. Yap, C. Schiepers, M. C. Fishbein, M. E. Phelps, J. Czernin, FDG-PET imaging in lung cancer: how sensitive is it for bronchioloalveolar carcinoma? *Eur J Nucl Med Mol Imaging* **29**, 1166-1173 (2002).
25. C. Scafoglio *et al.*, Functional expression of sodium-glucose transporters in cancer. *Proc Natl Acad Sci U S A* **112**, E4111-4119 (2015).
26. A. S. Yu *et al.*, Functional expression of SGLTs in rat brain. *Am J Physiol Cell Physiol* **299**, C1277-1284 (2010).
27. A. S. Yu *et al.*, Regional distribution of SGLT activity in rat brain in vivo. *Am J Physiol Cell Physiol* **304**, C240-247 (2013).
28. V. Kepe *et al.*, Positron emission tomography of sodium glucose cotransport activity in high grade astrocytomas. *J Neurooncol* **138**, 557-569 (2018).
29. N. Ishikawa, T. Oguri, T. Isobe, K. Fujitaka, N. Kohno, SGLT gene expression in primary lung cancers and their metastatic lesions. *Jpn J Cancer Res* **92**, 874-879 (2001).
30. D. B. Shackelford *et al.*, LKB1 inactivation dictates therapeutic response of non-small cell lung cancer to the metabolism drug phenformin. *Cancer Cell* **23**, 143-158 (2013).
31. Q. Bao, A. F. Chatziioannou, Estimation of the minimum detectable activity of preclinical PET imaging systems with an analytical method. *Med Phys* **37**, 6070-6083 (2010).
32. N. Suzawa *et al.*, Assessment of factors influencing FDG uptake in non-small cell lung cancer on PET/CT by investigating histological differences in expression of glucose transporters 1 and 3 and tumour size. *Lung Cancer* **72**, 191-198 (2011).
33. L. F. de Geus-Oei *et al.*, Biological correlates of FDG uptake in non-small cell lung cancer. *Lung Cancer* **55**, 79-87 (2007).
34. M. Mamede *et al.*, [18F]FDG uptake and PCNA, Glut-1, and Hexokinase-II expressions in cancers and inflammatory lesions of the lung. *Neoplasia* **7**, 369-379 (2005).
35. D. Devineni *et al.*, Pharmacokinetics and pharmacodynamics of canagliflozin, a sodium glucose co-transporter 2 inhibitor, in subjects with type 2 diabetes mellitus. *J Clin Pharmacol* **53**, 601-610 (2013).
36. C. J. Bailey, J. L. Gross, A. Pieters, A. Bastien, J. F. List, Effect of dapagliflozin in patients with type 2 diabetes who have inadequate glycaemic control with metformin: a randomised, double-blind, placebo-controlled trial. *Lancet* **375**, 2223-2233 (2010).
37. C. Ghezzi *et al.*, Dapagliflozin Binds Specifically to Sodium-Glucose Cotransporter 2 in the Proximal Renal Tubule. *J Am Soc Nephrol* **28**, 802-810 (2017).
38. M. Sala-Rabanal *et al.*, Revisiting the physiological roles of SGLTs and GLUTs using positron emission tomography in mice. *J Physiol* **594**, 4425-4438 (2016).

39. S. Sha *et al.*, Pharmacodynamic differences between canagliflozin and dapagliflozin: results of a randomized, double-blind, crossover study. *Diabetes Obes Metab* **17**, 188-197 (2015).
40. D. B. Shackelford *et al.*, mTOR and HIF-1alpha-mediated tumor metabolism in an LKB1 mouse model of Peutz-Jeghers syndrome. *Proc Natl Acad Sci U S A* **106**, 11137-11142 (2009).
41. C. Chen, N. Pore, A. Behrooz, F. Ismail-Beigi, A. Maity, Regulation of glut1 mRNA by hypoxia-inducible factor-1. Interaction between H-ras and hypoxia. *J Biol Chem* **276**, 9519-9525 (2001).
42. H. F. Bunn, R. O. Poyton, Oxygen sensing and molecular adaptation to hypoxia. *Physiological reviews* **76**, 839-885 (1996).
43. T. National Lung Screening Trial Research *et al.*, Reduced lung-cancer mortality with low-dose computed tomographic screening. *N Engl J Med* **365**, 395-409 (2011).
44. D. R. Aberle *et al.*, Results of the two incidence screenings in the National Lung Screening Trial. *N Engl J Med* **369**, 920-931 (2013).
45. M. K. Gould *et al.*, Recent Trends in the Identification of Incidental Pulmonary Nodules. *Am J Respir Crit Care Med* **192**, 1208-1214 (2015).
46. L. C. Horn L, Johnson DH. , Neoplasms of the Lung. *In: Kasper D, Fauci A, Hauser S, Longo D, Jameson J, Loscalzo J. eds. Harrison's Principles of Internal Medicine, 19e. New York, NY: McGraw-Hill* **http://accessmedicine.mhmedical.com/content.aspx?bookid=1130&Sectionid=69857702.** , (2015).
47. Y. Kobayashi, T. Mitsudomi, Management of ground-glass opacities: should all pulmonary lesions with ground-glass opacity be surgically resected? *Transl Lung Cancer Res* **2**, 354-363 (2013).
48. B. Chang *et al.*, Natural history of pure ground-glass opacity lung nodules detected by low-dose CT scan. *Chest* **143**, 172-178 (2013).
49. P. B. Bach *et al.*, Benefits and harms of CT screening for lung cancer: a systematic review. *Jama* **307**, 2418-2429 (2012).
50. K. A. van den Bergh *et al.*, Impact of computed tomography screening for lung cancer on participants in a randomized controlled trial (NELSON trial). *Cancer* **113**, 396-404 (2008).
51. R. Takahashi *et al.*, Early [18F]fluorodeoxyglucose positron emission tomography at two days of gefitinib treatment predicts clinical outcome in patients with adenocarcinoma of the lung. *Clin Cancer Res* **18**, 220-228 (2012).
52. K. C. Ho *et al.*, TLG-S criteria are superior to both EORTC and PERCIST for predicting outcomes in patients with metastatic lung adenocarcinoma treated with erlotinib. *Eur J Nucl Med Mol Imaging* **43**, 2155-2165 (2016).
53. J. Vansteenkiste, B. M. Fischer, C. Dooms, J. Mortensen, Positron-emission tomography in prognostic and therapeutic assessment of lung cancer: systematic review. *Lancet Oncol* **5**, 531-540 (2004).
54. V. Kepe *et al.*, Positron emission tomography of sodium glucose cotransport activity in high grade astrocytomas. *J Neurooncol*, (2018).
55. A. M. Loening, S. S. Gambhir, AMIDE: a free software tool for multimodality medical image analysis. *Mol Imaging* **2**, 131-137 (2003).
56. K.-Y. LIANG, S. L. ZEGER, Longitudinal data analysis using generalized linear models. *Biometrika* **73**, 13-22 (1986).

Acknowledgments

We thank Drs. Jason Lee, Charles Zamilpa and Tove Olafsen of the UCLA Crump Institute for Molecular Imaging for the constant support in performing the imaging experiments in mice, and the personnel of the UCLA Translational Pathology Core Laboratory for the procurement of human samples and processing of tissues. We thank Dr. Abigail Fletcher for careful reading of the manuscript. **Funding:** C.R.S. was supported by the following grants: NIH/National Center for

Advancing Translational Science (NCATS) UCLA Clinical and Translational Science Institute KL2 Translational Science Award, UL1TR001881; Integrated Molecular, Cellular, and Imaging Characterization of Screen-Detected Lung Cancer, NCI 1U01CA196408; American Cancer Society *Research Scholar Grant* 130696-RSG-17-003-01-CCE; Tobacco-Related Disease Research Program *High Impact Research Project Award* 2016TRDRP0IR00000143977; STOP Cancer Foundation Seed Grant; Saul Brandman Foundation grant. D.B.S. was supported by a Department of Defense Lung Cancer Research Program grant W81XWH-13-1-0459. S.M.D. was supported by NCI EDRN 1U01CA214182, NCI 1U01CA196408 and Merit Review Research Funds from the Department of Veterans Affairs. J.Y. was supported by Thoracic Surgery Foundation Research Award and STOP Cancer I.C.O.N./Natasha Girard Seed Grant.

Author contributions: D.B.S. and C.R.S. designed all the experiments, coordinated the work of all authors, and prepared the manuscript. C.R.S. performed the majority of experiments, including mouse imaging, therapeutic trials, and immunohistochemistry in mouse and patient tissues, and wrote the manuscript. B.V. performed immunohistochemistry in patient-derived xenograft tissues and PET imaging in GEMMs and PDXs. G.A. contributed to the establishment, maintenance, and imaging of the patient-derived xenografts and the imaging experiments. S.T.B. contributed to the establishment and maintenance of the genetically engineered mice. J.L. performed radiosynthesis of Me4FDG. A.S.S. facilitated the procurement of tissues. W.D.W. provided advice on the interpretation of clinical specimens and performed data analysis on human immunohistochemistry samples. C.E.M. performed data analysis on all the mouse samples. T.R.G. and D.E. performed all the statistical analyses. J.R.B. contributed to the design of experiments and provided advice on the tracer synthesis and interpretation of the data. J.Y. and D.R.A. provided advice on the selection of patients and provided critical feedback on the

manuscript. T.W. procured the human premalignancy specimens. S.M.D. provided advice and critical feedback on experiment planning and on the manuscript preparation. **Competing interests**: S.M.D. is on the Advisory Board of Early Diagnostics, Inc., T-Cure, and AstraZeneca. The tracer Me4FDG is covered by a UCLA patent application: Tracers for monitoring the activity of sodium/glucose co-transporters in health and disease. E.M. Wright, J.R. Barrio, B. Hirayama, and V. Kepe. IP filing date: 05/23/2006; 11/920,904; U.S. Patent 8,845,999. All other authors declare that they have no competing interests. **Data and materials availability**: All data associated with this study are present in the paper or supplementary materials. The models presented are available upon request to the corresponding authors after signing a material transfer agreement.

Figures

Fig. 1. SGLT2 is expressed in low-grade and GLUT1 in high-grade human lung adenocarcinoma

Immunohistochemistry was performed in human LADC samples with antibodies specific for SGLT2 and GLUT1. A) Invasive adenocarcinomas, different disease grades, as indicated. B) Quantification of SGLT2 (upper panel) and GLUT1 (lower panel) staining in different disease grades of LADC, measured by Jonchkeere-Terpstra test. ***$p < 0.001$. Scale bars: 50 μm. C) Normal alveoli. D) Pre-malignant lesions: atypical adenomatous hyperplasia, adenocarcinoma in situ, and minimally invasive adenocarcinoma. Scale bars: 50 μm (insert: 25 μm). E) Expression of SGLT2 and GLUT1 in different PDX models of LADC: well-moderately differentiated (PDX #004), moderately differentiated (PDXs #186 and #011), and poorly differentiated (PDX # 013). Scale bars: 50 μm.

Fig. 2. Glucose transporter expression and activity in lung adenocarcinoma is heterogeneous.

A) KP_{luc} mice were imaged with Me4FDG and FDG; the scatter plot reports the uptake of ROIs corresponding to single LADC nodules, expressed as percentage of injected dose per gram of tissue (%ID/g). The red box highlights tumors with high Me4FDG and low FDG uptake. The correlation was calculated using Pearson's coefficient (r). B) Representative transverse sections of the PET/CT images show three distinct tumor nodules, t1, t2, and t3. Uptake of Me4FDG is detectable in small nodules (t2 and t3), which are FDG-negative. C) Pearson correlation between Me4FDG uptake in lung adenocarcinomas and SGLT2 protein expression as measured by immunohistochemistry. The p-value was calculated from generalized estimating equation (GEE) models (*56*). D) Pearson correlation between SGLT2 and GLUT1 protein expression in regions of interest corresponding to small areas of the tumor which were clearly identified in the H&E

staining as purely low-grade or high-grade, as outlined in fig. S2F. The ROIs encompassing tumor areas with high-grade histology are reported as red circles, and the ROIs corresponding to low-grade tumor areas are represented by green triangles. E) Representative images of SGLT2 and GLUT1 expression in low- and high-grade tumor areas. Scale bars: 100 μm (inserts: 10 μm). F) Hematoxylin and eosin stain in an adjacent section shows the different morphology of the low- and high-grade tumor areas. Scale bars: 100 μm (inserts: 10 μm). G) SGLT2 and GLUT1 protein expression was compared between low- and high-grade tumors using GEE models. ***$p < 0.001$. H) Representative images of a human adenocarcinoma, adjacent slices of which were stained for SGLT2 (upper panel) or GLUT1 (lower panel). Scale bar: 1 mm. I) Higher magnification of a well-differentiated (blue squares) and a poorly differentiated (red squares) area of the samples presented in H. Scale bar: 100 μm.

Fig. 3. SGLT2 is expressed in early LADC and GLUT1 in advanced LADC in KP*luc* GEMMs

A) Schematic representation and whole-lung hematoxylin and eosin stain of LADC progression in KP*luc* mice at different time points after tumor induction, as indicated. Scale bar: 1 mm. B) Time course of SGLT2 and GLUT1 expression in KP_{luc} mouse lung lesions at different time points after tumor induction. Scale bar: 50 μm. C-D) Quantification of the SGLT2 (C) and GLUT1 (D) immunohistochemistry signal at different time points after tumor induction in KP_{luc} mice, measured by Jonchkeere-Terpstra test. *$p \leq 0.05$; ***$p \leq 0.01$. E) Time course of Me4FDG and FDG imaging in KP_{luc} mice. The first time point was taken when tumor nodules reached an average diameter of 7 mm, and the subsequent time points were performed at 2-week intervals. F-G) Quantification of Me4FDG (F) and FDG (G) signal in all 7 mice included in the cohort (with a total of 16 tumors). H-I) Schematic representation of glucose transporter expression in different stages of LADC: premalignant lesions and early-stage LADC express only SGLT2 (H), whereas

advanced tumors show spatial heterogeneity of glucose transport expression, with SGLT2 in well-differentiated and GLUT1 in poorly differentiated areas of the same tumor (I).

Fig. 4. SGLT2 inhibition delays development of lung adenocarcinomas in KP_{luc} GEMMs.
A-B) The effect of single-dose SGLT2 inhibitor dapagliflozin on SGLT activity was evaluated by Me4FDG PET. A) Representative 3D rendering of the PET/CT in the same KP_{luc} mouse imaged on different days with Me4FDG without or with co-injection of dapagliflozin. B) Comparison of Me4FDG uptake in n = 5 mice, expressed in percent of injected dose per gram of tissue (% ID/g) in regions of interest corresponding to single lung nodules (upper panel) and to the bladder (lower panel). Uptake was compared between groups using the two-sample t-test. ****$p < 0.0001$; **$p < 0.01$. C) Schematic representation of the therapeutic trials. GEMM: genetically engineered mouse model. AdenoCre: adenovirally encoded Cre recombinase. AAH: atypical adenomatous hyperplasia. ADC: adenocarcinoma. D-J) Therapeutic trial in KP_{luc} mice treated with placebo or canagliflozin starting 2 weeks after tumor induction and carried on for either 6 weeks (Week 8 cohort) or up to 3 months (Survival cohort). D) Representative images of bioluminescence in two mice belonging to the two treatment groups. E) Quantification of the bioluminescent signal in the two therapeutic groups over time. The p-value presented was from the interaction term between time/group from a generalized estimating equation (GEE) model (*56*). F) Representative hematoxylin and eosin stain of mouse lungs in the two treatment groups from both trials. Scale bar: 5 mm. G) Quantification of the tumor area in the Week 8 and Survival cohorts. Tumor size was compared between placebo and canagliflozin groups using the two-sample t-test. *$p < 0.05$. H-I) Ki67 staining in premalignant lesions: H) representative images; I) quantification of the signal in the two groups. The groups were compared using t-test. Scale bars: 50 μm. J) Overall survival

curves for each group were constructed using the Kaplan-Meier method and formally compared using the log-rank test.

Fig. 5. SGLT2 inhibition of Me4FDG positive LADC slows down tumor growth in patient-derived xenografts (PDXs).

A) The mice carrying PDXs were treated with 30 mg/kg canagliflozin for 1 month. They were imaged with Me4FDG and FDG PET/CT one day before and two weeks after the beginning of treatment; in addition, the mice received weekly CT scans to monitor tumor growth. B) Final tumor volumes on the last day of the trial, as measured by CT; the groups were compared using a linear mixed effects model for log (volume) with adjustment for trial and mouse random effects.

C-G) Results of the Me4FDG PET imaging in the mice included in the therapeutic trial. C) Representative PET/CT images in transversal section of two mice, one in the placebo and one in the canagliflozin group, injected with Me4FDG before (day 0) and after (week 2) the beginning of the treatment. The Me4FDG scans presented are from the same two mice. White arrows: tumor. Yellow arrowhead: bladder. D) Quantification of Me4FDG uptake in the tumors, expressed as percentage of injected dose per gram of tissue, in all the mice included in the trial, measured by t-test. ***$p < 0.001$, **$p < 0.01$. E) Correlation between pre-treatment Me4FDG uptake in the tumors in the placebo group and the fold increase in volume from the beginning to the end of the therapeutic trial. Pearson's correlation coefficient (r) and p-value are reported. F) Correlation between pre-treatment Me4FDG uptake in the tumors in the canagliflozin group and the fold increase in volume from the beginning to the end of the therapeutic trial. Pearson's correlation coefficient (r) and p-value are reported. G) Correlation between the percent change in Me4FDG uptake from the beginning to week 2 of the therapeutic trial and the fold increase in volume from the beginning to the end of the therapeutic trial; Pearson's correlation coefficient (r) and p-value

are reported. H-L) Results of the FDG PET imaging in the mice included in the therapeutic trial. The panels report the data relative to FDG uptake in the same mice presented in C-G. H) Representative PET/CT images in transversal section. White arrows: tumor. I) Quantification of FDG uptake in the tumors (n.s.: not significant). J) Correlation between pre-treatment FDG uptake in the tumors in the placebo group and the fold increase in volume. K) Correlation between pre-treatment FDG in the canagliflozin group and the fold increase in volume. L) Correlation between the percent change in FDG uptake and the fold increase in volume from the beginning to the end of the therapeutic trial.

Table 1. Clinical characteristics of the patients with atypical adenomatous hyperplasia included in the study.

Pathology ID	Age	Sex	Smoking Status	Pack-Years	Means of Detection	Pathological Stage	Overall Stage
S04-06316	58	M	Current	40	Incidental	T1aN0M0	IA
S07-06119	59	M	Former	60	Symptomatic	T3N0M0	IIB
S08-00530	54	F	Never	0	Symptomatic	TisN0M0	0
S10-02063	73	F	Former	31	Screening CXR	T1aN0M0	IA
S11-00793	82	F	Never	0	Incidental	T1aN0M0	IA
S11-07781	75	F	Former	20	Incidental	T3N0M0	IIB
S11-16172							
S12-04286	77	M				T1bN0M0	IA
S13-07409	70	F	Former	28	Surveillance	T3N0M0	IIB

Type of file: figure
Label: Figure 1
Filename: Fig.1_PMC.tif

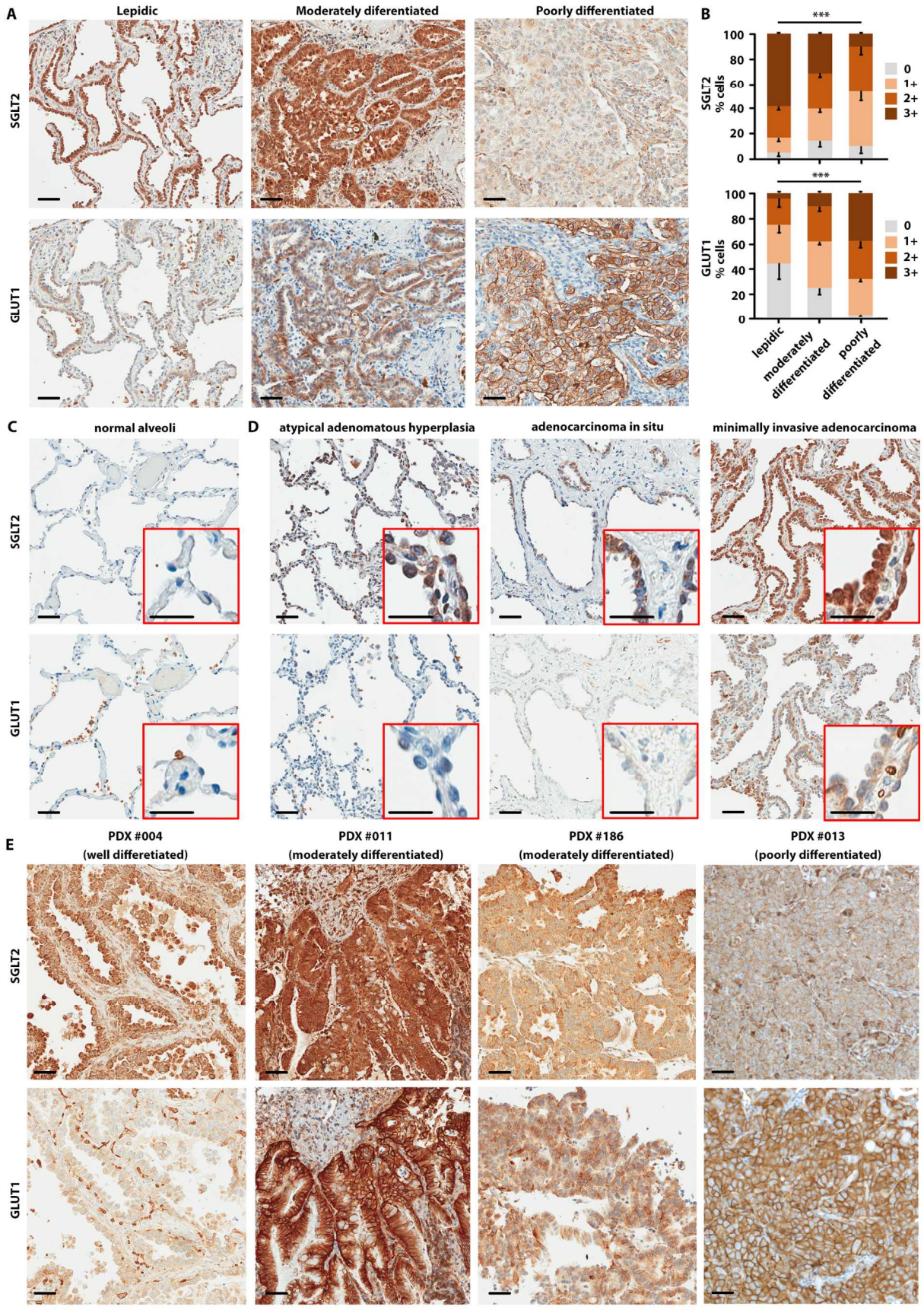
A
Lepidic
Moderately diferentiated
Poorly differentiated
SGLT2
GLUT1
B
***
SGLT2 % cells
GLUT1 % cells
0
1+
2+
3+
lepidic
moderately differentiated
poorly differentiated
C
normal alveoli
D
atypical adenomatous hyperplasia
adenocarcinoma in situ
minimally invasive adenocarcinoma
E
PDX #004
(well differetiated)
PDX #011
(moderately differentiated)
PDX #186
(moderately differentiated)
PDX #013
(poorly differentiated)

Type of file: figure
Label: Figure 2
Filename: Fig.2_PMC.tif

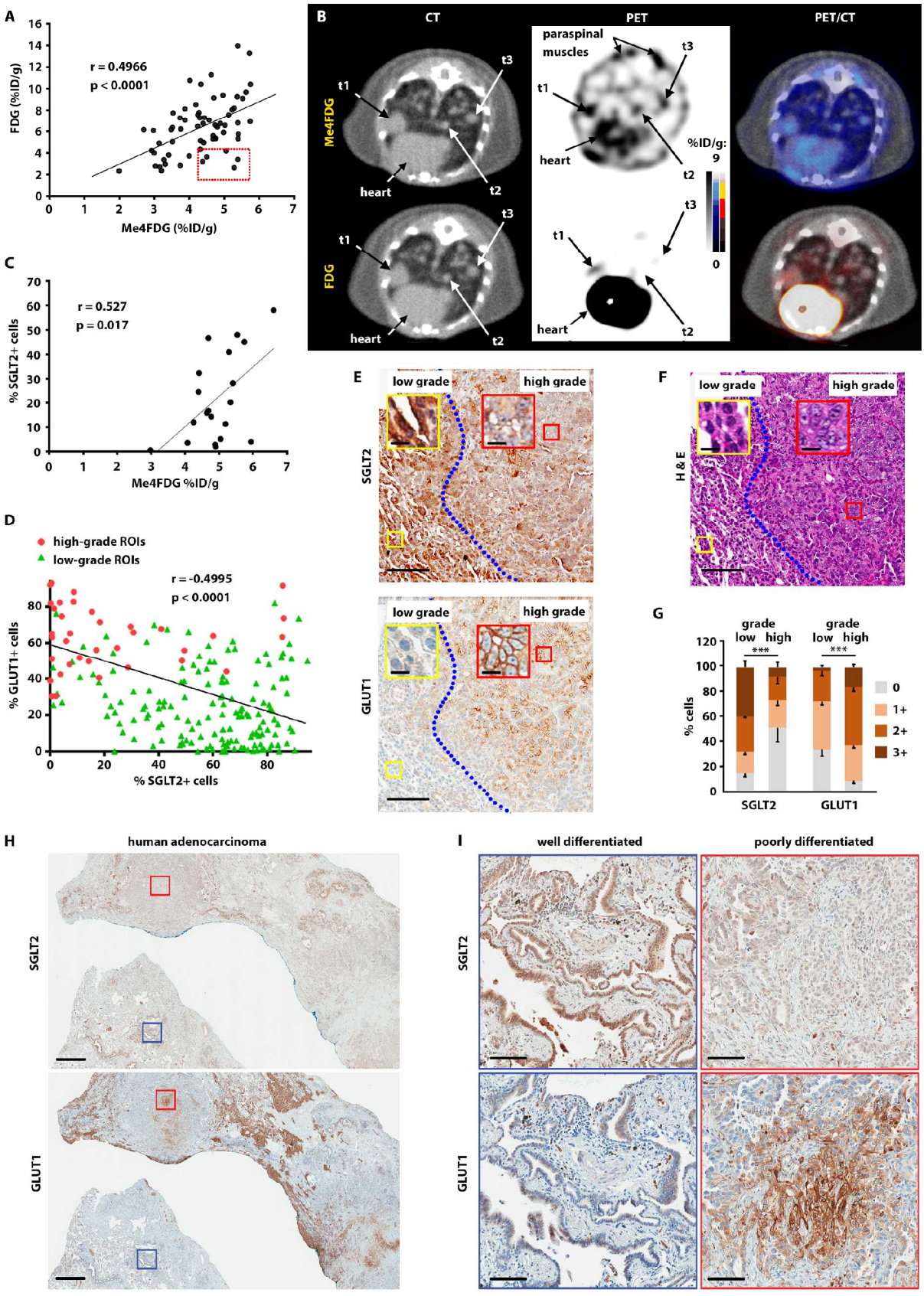
A
FDG (%ID/g)
Me4FDG (%ID/g)
r = 0.4966
p < 0.0001
B
CT
PET
PET/CT
Me4FDG
FDG
t1
t2
t3
heart
paraspinal muscles
%ID/g:
9
0
C
% SGLT2+ cells
Me4FDG %ID/g
r = 0.527
p = 0.017
D
high-grade ROIs
low-grade ROIs
% GLUT1+ cells
% SGLT2+ cells
r = -0.4995
p < 0.0001
E
low grade
high grade
SGLT2
GLUT1
F
H & E
G
grade
low high
***
% cells
0
1+
2+
3+
SGLT2
GLUT1
H
human adenocarcinoma
SGLT2
GLUT1
I
well differentiated
poorly differentiated
SGLT2
GLUT1

Type of file: figure
Label: Figure 3
Filename: Fig.3_PMC.tif

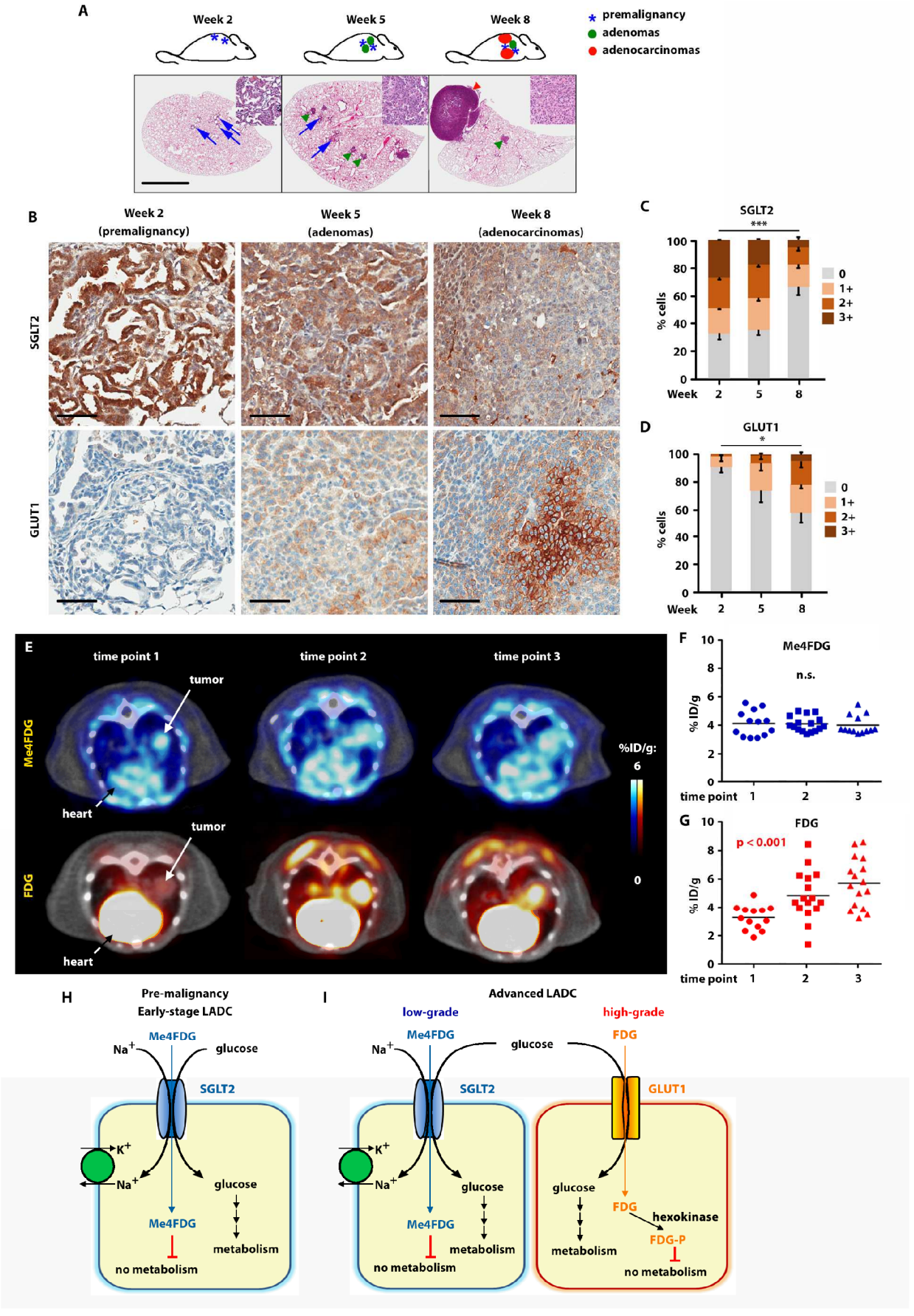
A
Week 2
Week 5
Week 8
premalignancy
adenomas
adenocarcinomas
B
Week 2 (premalignancy)
Week 5 (adenomas)
Week 8 (adenocarcinomas)
SGLT2
GLUT1
C
SGLT2
***
% cells
Week
0
1+
2+
3+
D
GLUT1
*
E
time point 1
time point 2
time point 3
Me4FDG
FDG
tumor
heart
%ID/g:
6
0
F
Me4FDG
n.s.
% ID/g
time point
G
FDG
p < 0.001
H
Pre-malignancy
Early-stage LADC
Me4FDG
glucose
SGLT2
metabolism
no metabolism
I
Advanced LADC
low-grade
high-grade
FDG
GLUT1
hexokinase
FDG-P

Type of file: figure
Label: Figure 4
Filename: Fig.4_PMC.tif

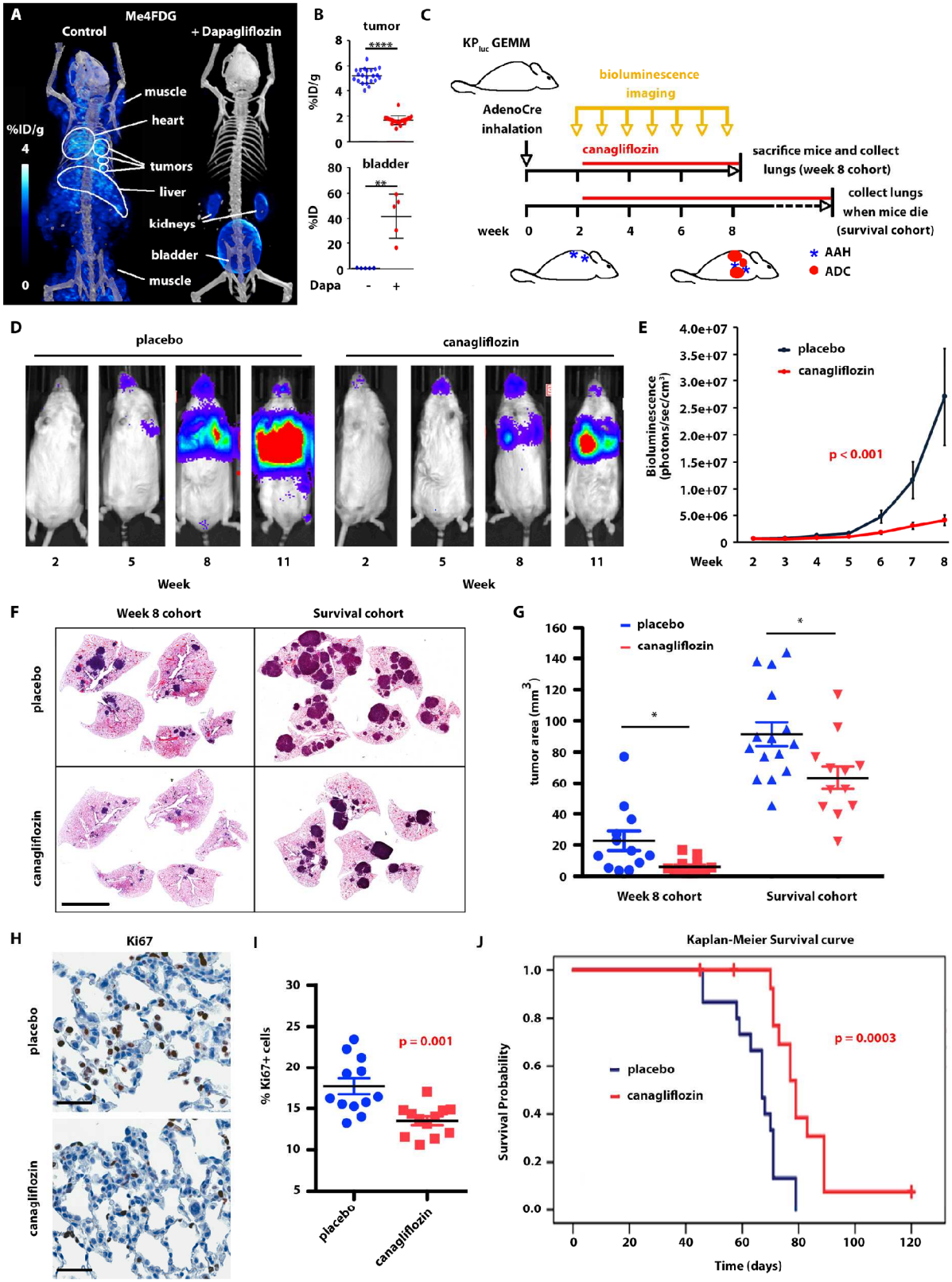
A
Me4FDG
Control
+ Dapagliflozin
%ID/g
4
0
muscle
heart
tumors
liver
kidneys
bladder
muscle
B
tumor
%ID/g
****
bladder
%ID
**
Dapa
C
KP luc GEMM
bioluminescence imaging
AdenoCre inhalation
canagliflozin
sacrifice mice and collect lungs (week 8 cohort)
collect lungs when mice die (survival cohort)
week
AAH
ADC
D
placebo
canagliflozin
Week
E
placebo
canagliflozin
Bioluminescence (photons/sec/cm²)
p < 0.001
Week
F
Week 8 cohort
Survival cohort
placebo
canagliflozin
G
placebo
canagliflozin
tumor area (mm³)
Week 8 cohort
Survival cohort
H
Ki67
placebo
canagliflozin
I
% Ki67+ cells
p = 0.001
placebo
canagliflozin
J
Kaplan-Meier Survival curve
Survival Probability
p = 0.0003
placebo
canagliflozin
Time (days)

Type of file: figure
Label: Figure 5
Filename: Fig.5_PMC.tif

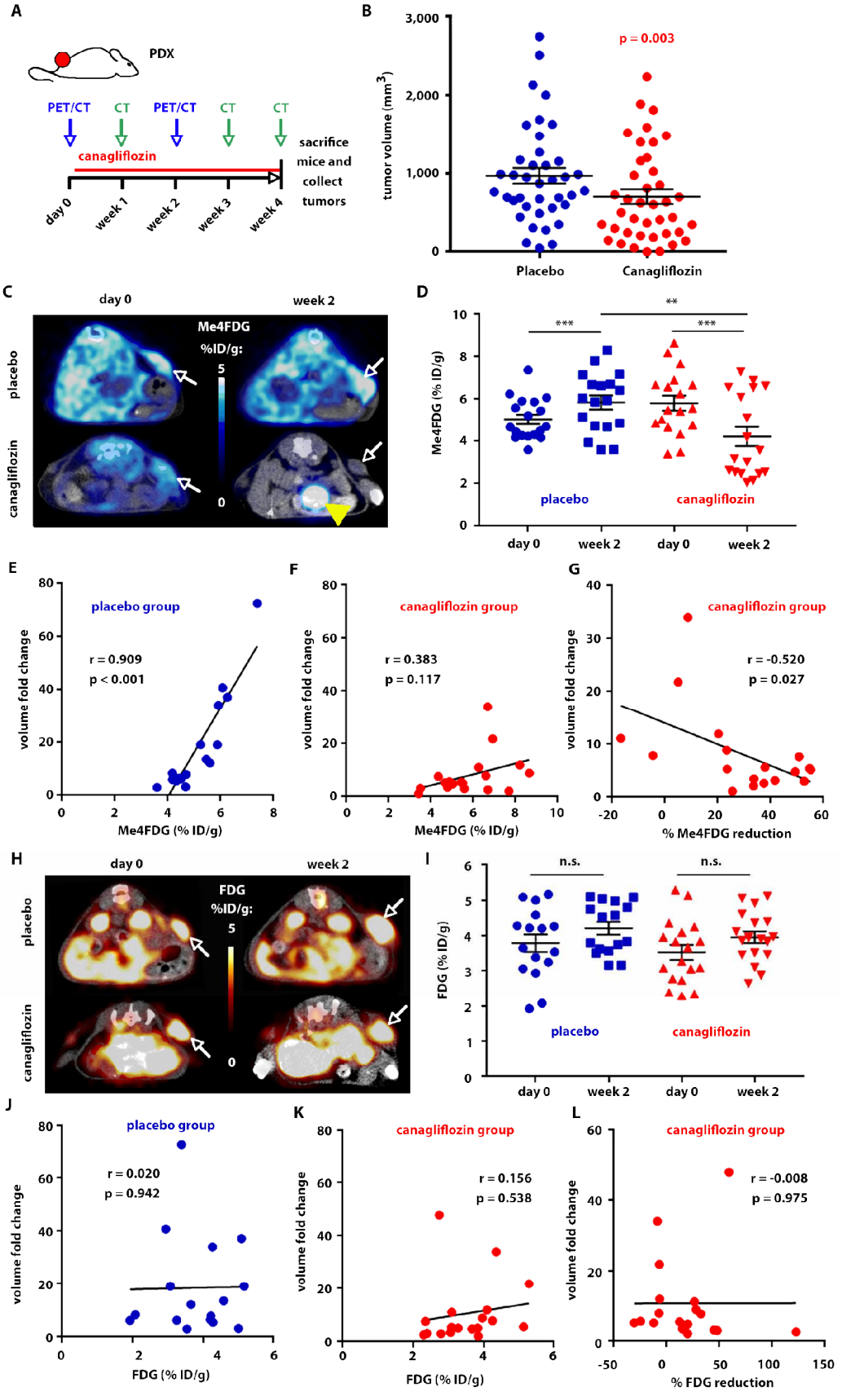
A
PDX
PET/CT
CT
PET/CT
CT
CT
canagliflozin
sacrifice mice and collect tumors
day 0
week 1
week 2
week 3
week 4
B
p = 0.003
tumor volume (mm3)
3,000
2,000
1,000
0
Placebo
Canagliflozin
C
day 0
week 2
Me4FDG
%ID/g:
5
0
placebo
canagliflozin
D
Me4FDG (% ID/g)
***
**
***
placebo
canagliflozin
day 0
week 2
day 0
week 2
E
placebo group
r = 0.909
p < 0.001
volume fold change
Me4FDG (% ID/g)
F
canagliflozin group
r = 0.383
p = 0.117
volume fold change
Me4FDG (% ID/g)
G
canagliflozin group
r = -0.520
p = 0.027
volume fold change
% Me4FDG reduction
H
day 0
week 2
FDG
%ID/g:
5
0
placebo
canagliflozin
I
FDG (% ID/g)
n.s.
n.s.
placebo
canagliflozin
day 0
week 2
day 0
week 2
J
placebo group
r = 0.020
p = 0.942
volume fold change
FDG (% ID/g)
K
canagliflozin group
r = 0.156
p = 0.538
volume fold change
FDG (% ID/g)
L
canagliflozin group
r = -0.008
p = 0.975
volume fold change
% FDG reduction

The NIHMS has received the file 'aat5933_Supplement_PMC.docx' as supplementary data. The file will not appear in this PDF Receipt, but it will be linked to the web version of your manuscript.